Photocurable 3D printed anisotropic electrically conductive materials based on bio-renewable composites

1. Introduction

The global situation regarding the overwhelming consumption of fossil fuel-based materials points out the need for a revolution in the utilization of raw materials in order to move towards a green and sustainable economy [1]. Thus, plant-based and other renewable resources obtained materials are the main mobilizers of changes within the manufacturing industry [2,3].

Along with the circular economy, the technological growth in the world alludes to a fourth industrial revolution or Industry 4.0 and to an interconnected world based on communication systems, sensor and actuator devices, enabling the Internet of Things (IoT) paradigm [4]. This technological revolution is accompanied by what is known as Additive Manufacturing (AM), alias 3D printing, which enables the fabrication of different products with desirable (potentially complex) three-dimensional shapes by the layer-by-layer deposition of materials according to a virtual model that is digitally sliced, i.e, it does not require moulds or machining [5,6]. Despite printing technologies being much improved over time, the materials that have commonly been used with them have not evolved significantly. Thus, the AM methods that are found nowadays are mostly based on non-renewable materials. In this way, to properly achieve both digitalization and sustainability, the 3D printing of sensors and actuators based on materials with natural or renewable origin becomes mandatory [7,8].

Among the different 3D printing technologies, those based on UV light curing or photopolymerization can be highlighted. Photopolymerization is defined as the synthesis of polymers by chain reactions that are initiated upon the absorption of UV or visible light converting

thus liquid solventless formulations into solid materials [9] and presents advantages with respect to other printing technologies such as rapid solidification, room curing temperatures, small volumes of volatile organic compounds and high energy processing efficiency, among others [10]. However, currently available UV curing 3D printing technologies do not allow the use of directly obtained bio-based materials, that must be previously modified in order to adjust them to the optimal printing conditions in terms of reactivity and/or viscosity [11,12]. At this point, bio-based oils modified through epoxidation and/or acrylation highlight as widely used materials in 3D printing, including soybean, canola, sunflower, sesame and olive oils. It has been demonstrated that these five acrylated oils present good characteristics to be used in digital light processing (DLP) printing in terms of penetration depth and critical exposure. Further, their 3D printed parts present a quality comparable to commercially available inks. Furthermore, sunflower and canola oil-based materials are identified as the most promising candidates in terms of price, curing behaviour, resolution, and mechanical properties, being thus able to be printed in complex geometries [13]. Particularly, soybean oil-based has been demonstrated to be suitable for Optical 3D printing in the scales from nano- to macro-dimensions, which can be processed even without the addition of photoinitiator [14].

Although the suitability of bio-based oils for photocurable 3D printing has been demonstrated with results very close to those obtained with materials of non-biorenewable origin, those polymers by themselves do not have the necessary functional requirement to be used in many sensor and actuator applications. Therefore, polymer-based composites, in which a filler capable of adding a specific functionality to the system is used together with a polymer that provides specific physico-chemical properties and processability to the system, are commonly used [10]. In this sense, bio-based photopolymers have not been yet properly investigated while petroleum-based ones include conductive, piezoresistive, piezoelectric, thermochromic or photoluminescent materials, among others, obtained by adding fillers such as multiwalled carbon nanotubes (MWCNT) [15], ZnO nanostructures [16], bis(1-butyl-3-methylimidazolium) tetrachloronickelate ($[Bmim]_2[NiCl_4]$) ionic liquid [17] or $[Cu_4I_4(PPh_3)_4]$ and $[Cu_4I_4(PPh_2(CH_2)_2CH_3)_4]$ copper iodide clusters [18].

Specifically, electrically conductive materials presenting anisotropy have great relevance in sensor application in areas such as smart robotics [19], human motion detection [20] and multidimensional wearable electronics [21]. Further, the formation of directional electrically conductive pathways, allows increasing the electrical conductivity using less amount of conductive fillers and can favour the mechanical properties [22]. This mentioned orientation and arrangement of the electrically conductive fillers is not easy to obtain and is controlled primarily by the process involved in the 3D printing technique or by an external stimulus that can induce filler orientation during printing [23] such as a magnetic or electric field, mechanical stretching or shear force [24]. This has been achieved in some studies in which different particles, including aluminium, titanium, copper, magnetite nanoparticles, and carbon nanofibers have been assembled with acoustic field during stereolithography 3D printing for the fabrication of embedded conductive wires and other patterns within 3D structures [25,26]. Moreover, by the use of femtosecond pulsed laser beam (fs laser beam) within two-photon polymerization lithography, the 3D microfabrication of single-wall carbon nanotube/polymer composites can be achieved [27] as well as the assembly of aligned carbon nanotubes in three dimensions for multifunctional device fabrication [28]. This fs laser beam has been also employed for precise assembly and joining of silver nanowires in three dimensions for highly conductive composite structures presenting ~200 nm resolution structures [29]. However, to our knowledge, electrical anisotropy has not been already obtained both from bio-renewable origin materials and by digital light processing (DLP) 3D printing technique, despite its environmental and technological interest.

In this scope, the present work reports on the development of bio-renewable electrically conductive materials obtained by 3D printing of a natural-based polymer composite. Acrylated epoxidized soybean oil (AESO) was used as a matrix together with MWCNT as functional filler. The obtained composites were characterized in terms of physico- chemical properties and electrical conductivity as a function of the filler content and printing conditions. Different 3D printed structures were obtained to demonstrate the suitability of the materials for applications.

2. Materials and methods

2.1. Materials and sample preparation

Acrylated epoxidized soybean oil (AESO) that contains 4000 ppm of monomethyl ether hydroquinone as inhibitor and isobornyl methacrylate (IBOMA) of technical grade were purchased from Sigma Aldrich and used as received. Phenyl bis(2,4,6-trimethylbenzoyl) phosphine oxide, also named as Irgacure 819 or BAPO, was purchased from BASF and used as photoinitiator. Poly(ethylenglycol) diacrylate, PEGDA, with a molecular weight of 575 g mol^{-1} was purchased from Sigma Aldrich and used as sacrificial materials during 3D printing process, together with a 1 phr of BAPO photoinitiator. Ethanol (EtOH), from Merck, with 96% of purity was used as solvent for sample cleaning. Multi-walled carbon nanotubes (MWCNT) with reference NC7000™, purity of ≈ 90%, average diameter ≈ 9.5 nm, and average length ≈ 1.5 μm were provided by Nanocyl, S.A, Belgium and used as conductive filler.

In order to determine the best formulation for 3D printing, a batch of samples were prepared by mixing the AESO with IBOMA in different ratios form 100:0–50:50 (in wt%). Samples were mixed by magnetically stirring (AREC Heating Magnetic Stirrer from VELP SCIENTIFICA) at 60ºC for 30 min. Then, 1 phr of Irgacure 819 photoinitiator was added to the formulation, which was stirred again for other 30 min at same temperature. In order to obtain a homogeneous solution, all formulations were degassed by ultrasonic bath for 30 min at 50ºC. Then, photocured samples were prepared by placing the formulations on silicon molds to achieve rectangle samples of 20 × 7.5 mm^2 and a thickness of 500 μm after curing by illumination with a DYMAX ECE 5000-UV lamp during 60 s at 130 mw/cm^2.

The prepared samples are summarized in Table 1, where bio-renewable carbon (BRC) content was calculated considering the BRC contents of both biorenewable materials (AESO and IBOMA) and applying Eq. (1):[30].

$$BRC\ (\%) = \frac{Biosourced\ \ Carbon}{Total\ \ Carbon} x100 \quad (1)$$

For electrically conductive composite materials, the corresponding amount of carbonaceous filler was added to AESO:IBOMA formulations to obtain samples with a MWCNT concentration ranging from 0 to 0.6 wt%. To promote a good dispersion and disentanglement of MWCNT, the samples were homogenized using magnetic stirring for 2 h at 60ºC and ultrasonic bath (GT sonic from ORMA-Eurotek) for 1.5 h at 50ºC. After complete dissolution, photocured samples were prepared following the same procedure as for pristine materials obtaining here samples with dimensions of 20 × 7.5 × 0.25 mm^3.

In the case of sample 3D printed samples, they were obtained by

Table 1
Composition and biorenewable carbon (BRC) content of the prepared pristine polymer formulations.

Name	Amount of AESO (wt%)	Amount of IBOMA (wt%)	Amount of photoinitiator (phr)	BRC (%)
A	100	0	1	85.1
B	90	10	1	83.6
C	80	20	1	82.1
D	70	30	1	80.7
E	60	40	1	79.2
F	50	50	1	77.7

using the 0.6 wt% MWCNT containing formulation with 50:50 wt% of AESO:IBOMA. As a 3D printer the commercial DLP printer from ASIGA, model ASIGA PICO 2 HD with a nominal pixel resolution of 39 μm and a light emission at λ = 385 nm was employed. The layer thickness and UV light intensity were fixed at 50 μm and 35 mW/cm^2, respectively, and the exposure time per layer was fixed at 8 s for all printed samples. The working temperature for the 3D printer was 40ºC and the approach velocity of the platform was minimal (1.5 mm/s).

Finally, the printed objects were sonicated in ethanol for 5 min to remove the unreacted monomers and then post-cured under UV-light using a medium-pressure mercury lamp provided by Robot Factory (3 min, 12 mw/cm^2).

The evaluation of the precision of the printing process, i.e., the accuracy, was measured throughout the shape fidelity of the printed object to the reference CAD by means of a 3D scan of the samples and comparing the digital file and the scan of 3D printed object obtained at the CA Analyzer program of the 3Shape scanner model E3.

Topographical analysis of 3D printed samples was performed by optical microscopy (Olympus BX53MRF-S) and profilometry (KLA Tencor D-100) at three different positions in three faces of the filled cube. For profilometry, a stylus force of 0.03 mg in a total distance of 5 mm and at a scan velocity of 0.1 mm/s was employed. In addition, surface roughness of the 3D printed cube was calculated using atomic force microscopy (AFM). A NX10 AFM from Park Systems was operated in non-contact mode using PPP-NCHR probes (nominal force constant of 42 N/m and resonance frequency of 330 kHz) from Nanosensors. The topography images obtained were processed using Gwyddion and cor- rected using a second order polynomial background correction. For each image, the root-mean-square roughness (R_q) was calculated using Gwyddion. The R_q roughness is defined according to Eq. (2) as:

$$R_q = \sqrt{\frac{1}{N}\sum_{i=1}^{N}(z_i - \bar{z})} \quad (2)$$

Where N is the total number of points of the image, z_i the height of each point and $\bar{z}$ is the mean height. Then, the average value and standard deviation of the roughness was computed using the roughness calculated for each image.

2.2. Sample characterization

2.2.1. Characterization of the formulations

The photocuring reaction of the prepared formulations was evaluated by real-time photorheology using an Anton PAAR Modular Compact Rheometer (Physica MCR 302, Graz, Austria) equipped with a Hamamatsu LC8 lamp that generates the UV light and irradiates the sample from the bottom part with an irradiance intensity of 30 mW/ cm^2. The measurements were carried out in parallel-plate configuration with a glass bottom plate and an upper disk of 25 mm of diameter maintaining a distance between them of 0.3 mm (0.15 mm in case of composite samples). The tests were performed at constant frequency of 1 Hz and at temperature of 25 ºC. The UV light was switched on after 60 s to let the system stabilize before the onset of photopolymerization reaction. The obtained results were averaged after three measurements for each sample.

The total double bond conversion of different AESO:IBOMA formulations and MWCNT/AESO:IBOMA composites was monitored using an ATR-FTIR equipment and by the disappearance of the acrylic double bond peak located at 1635 cm^{-1} [31]. For that, samples were firstly measured in liquid state (pre-cured) and then in solid state (post-cured) after being irradiated for 90 s at room temperature and under nitrogen to 600 cm^{-1} at a resolution of 4 cm^{-1}.

Viscosity measurements were performed with an Anton PAAR Modular Compact Rheometer (Physica MCR 302, Graz, Austria) using a cone-plate geometry CP50–1 with a fixed gap of 1 mm. The cone presented a diameter of 25 mm and cone-angle of 1º. All experiments were performed using a constant volume of each sample and at fixed temperature of 25ºC. The viscosity of the samples was recorded varying the shear rate from the lowest value of 0.01 s^{-1} to the highest value of 1000 s^{-1}. The averaged results of each sample after three measurements are presented.

2.2.2. Characterization of the crosslinked materials

Dynamic mechanical thermal analysis (DMTA) measurements were performed in all prepared photocured rectangular samples using a Tritec 2000 DMA equipment from Triton Technology Ltd. The tests were carried out at a frequency of 1 Hz and with a total displacement of 20 μm varying the temperature from — 80ºC to 180ºC in a temperature ramp of 2ºC/min. The apparent crosslinking density (v_c) was calculated according to the Eq. (3):[32].

$$v_c = \frac{E'_R}{3RT} \quad (3)$$

where v_c is the crosslinking density in number of moles of network chains per unit volume of the network, E'$_R$ is the storage modulus value at the rubbery plateau, R is the gas constant and T the absolute temperature.

The quality of the 3D printed samples prepared with 0.6 wt% MWCNT and 50:50 wt% of AESO:IBOMA was characterized by 3D scanning of the printed objects with different shapes. 3D scanning was performed with a E3 3D scanner from 3Shape (Copenhagen, Denmark) and heat map of differences between the digital files and the digitalization of the real objects created by 3D scanner was reported.

The dispersion of MWCNT in the different composites was studied by Scanning Electron Microscopy (SEM) analysing the cross-section of the cold fractured samples using a Hitachi S-4800 microscope at an accelerating voltage of 5 kV with a magnification range from 60 × to 20000 × . In all cases, samples were previously coated with a 20 nm gold layer with a sputtering Polaron SC502 apparatus.

The electrical conductivity (σ) of the composites was obtained with an automated Keithley 487 picoammeter/voltage source by measuring the voltage/current (I-V) curves applying voltages between — 10 to + 10 V with a step of 1 V. The electrical conductivity was determined from the obtained resistance (R) and the geometrical characteristics of the samples, following Eq. (4):[31].

$$\sigma = \frac{l}{RA} \quad (4)$$

atmosphere using a Dymax ECE 5000 UV lamp at an irradiance of 130 mW/cm^2. For each measurements the Thermo Scientific Nicolet iS50 FTIR Spectrometer equipped with a diamond crystal ATR accessory was used and 32 spectra were obtained in the spectral range from 4000

where A is the area of electrodes and *l* is the thickness of the composites. In the case of photocured materials, the composites were previously gold-coated using sputtering Polaron SC502 with circular contacts of 5 mm of diameter deposited on both sides of the samples. In the case of 3D printed samples, copper wire electrodes were placed onto the spec- imens using a silver conductive paste to reduce contact resistance. The σ values are provided as the average values of 3 measurements.

3. Results and discussion

3.1. Optimization of the polymer matrix

3.1.1. Study of the photocurable formulations

Several formulations containing different ratio of acrylated epoxidized soybean oil (AESO) -the crosslinking agent- and isobornyl methacrylate (IBOMA) - the reactive diluent- were prepared as indicated in the experimental section. By changing the quantity of reactive diluent, it is possible to tailor both the physico-chemical properties of synthetized

materials as well as the viscosity and photoreactivity of the photocurable formulations, which are critical factors in terms of 3D printability.

Initially, the photopolymerization processability of the different polymer formulations was evaluated using real-time photorheology, where the evolution of both storage (G') and loss (G'') modulus were measured while samples were illuminated under UV light of 405 nm. Fig. 1a represents the G' values as a function of irradiation time for all prepared samples while Table 1 collects the values of curing rate (ΔG'/Δt), measured as the slope of the curve in the initial irradiation times, and the gel time (t_{gel}), which is the time needed to achieve the gelation of each sample and that is obtained as the crossover between G' and G'' moduli.

The photorheology curves of all samples present a similar trend. Independently of the reactive diluent content, identified by a sharp increase of the G' when light is switched on, followed by a plateau after several seconds of light illumination. When IBOMA is further increased, the t_{gel} is maintained almost constant and at around 1.5 s, indicating the suitable photopolymerization reaction independently on the reactive diluent content. In addition, the curing rate of the samples slightly increases from 44.5 ± 1.1–54.3 ± 1.6 kPa/s. The increase in the photoreactivity of the formulation with increasing IBOMA content is thus ascribed to the effect of the reactive diluent on the viscosity of formulations, particularly, the low in situ viscosity during the initial stages of the reaction [33]. Furthermore, the effect of IBOMA addition on the

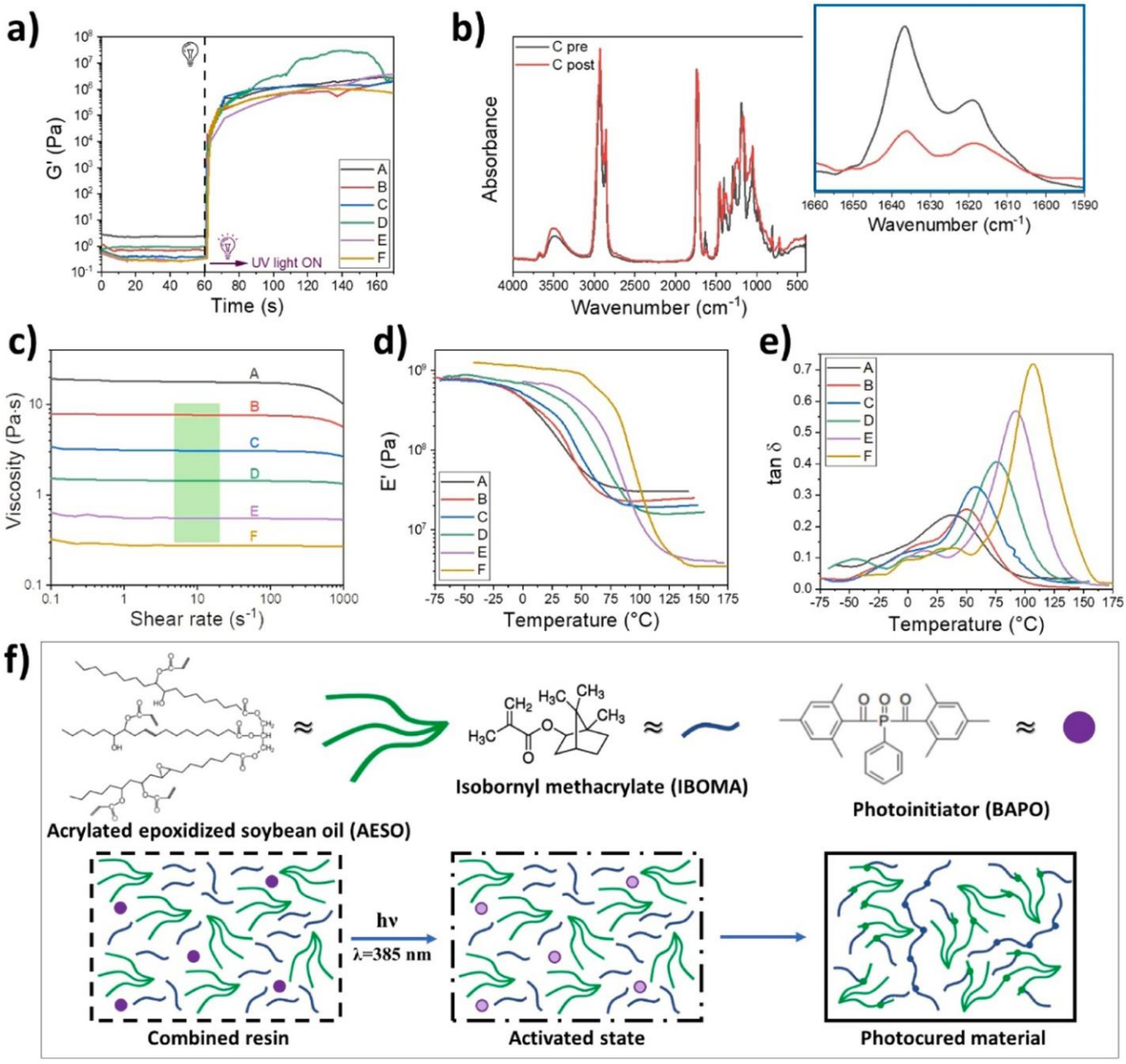

Fig. 1. a) Photorheology plots corresponding to the evolution of the storage modulus (G') of formulations containing different AESO:IBOMA ratios. b) FTIR spectra for AESO:IBOMA 80:20 ratio sample before (pre) and after (post) irradiation with UV-light, showing the double bond conversion. c) Viscosity curves of formulations containing different AESO:IBOMA ratios (the area in green represents the viscosity range recommended for DLP inks and the estimated range of shearing during printing). d) Storage modulus and e) tan δ curves for photocured AESO:IBOMA samples at different ratios. f) Schematic diagram of the photocurable mechanism of the AESO:IBOMA resin.

initial viscosities of the formulations can be related to the decrease of the G′ values before the onset of photopolymerization [34] and will be later characterized.

The photopolymerization process was also investigated by FTIR, where the acrylic double bond (C⁻C) conversion was measured following the decrease of the corresponding peak at 1635 cm^{-1} [31]. Fig. 1b depicts all FTIR spectra of sample C (Table 1) as a representative example together with the magnification of the zone corresponding to the double bond peak for both pre-exposure and post-exposure measurements. Table 2 collects the obtained FTIR conversion values.

The FTIR spectra of AESO displays the characteristic peaks ascribed to the main functional groups present in the triglyceride-based molecule. Thus, stretching vibrations of different groups such as -OH, C⁻O and C-O-C corresponding to the ester group of the acrylated epoxidized oil are shown at 3460, 1730 and 1160 cm^{-1}, respectively. Further, the corresponding peaks of the backbone of triglyceride can be appreciated at 2920, 2850 and 1450 cm^{-1}, directly related to the asymmetric stretching vibrations and deformations of the C-H bond in the $-CH_2-$ and $-CH_3-$ groups. In addition, the presence of the functionalized groups, i. e, the acrylic double bond groups, can be also observed by the bands located at 1635 and 810 cm^{-1} [35]. When samples are irradiated, the success of the photopolymerization was confirmed by the decrease of the double bond peak as it is clearly observed in magnified region of the spectra. This double bond conversion is maintained almost constant when IBOMA is added and all the investigated photocurable formulations present a final FTIR conversion values around 77%, which agrees with related studies based on the same AESO material [31].

The viscosity of the prepared formulations was then characterized as it is an important parameter to be evaluated in 3D printing process, the rheological behaviour notably affecting printing characteristics and performance [36]. Fig. 1c depicts the viscosity curves for all prepared formulations in the shear rate range from 0.1 to 1000 s^{-1} while Table 2 summarizes the viscosity values of each sample obtained at a shear rate of 10.

The AESO-based materials present a Newtonian behaviour characterized by a constant value of the viscosity in all the studied shear rate range. When IBOMA is added, AESO viscosity is strongly decreased of 2 order of magnitude being 18.2 ± 1.1 Pa·s for pure AESO and as low as 0.28 ± 0.01 PA·s for the sample containing higher IBOMA content. All the rest of the samples present intermediate values between them, showing a linear decrease of viscosity of the formulation by increasing IBOMA content. In fact, the effect of increasing reactive diluent has been also reported in literature for AESO resin in the presence of other reactive diluents such as methacrylated fatty acid or methacrylated eugenol [37].

The viscosity range recommended in the literature for DLP inks is between 0.2 and 10 Pa·s, while shear rates of 5 and 20 s^{-1} indicates the estimated range of shearing during the printing process [13]. Thus, the addition of just 10 wt% of IBOMA diluent to AESO is enough to achieve an appropriate viscosity value in all necessary shear rate range for DLP printing. Also, the addition of 50 wt% of IBOMA leads to a formulation capable to be DLP printable. However, considering the intention of adding fillers to the polymeric formulations, the sample B containing 10 wt% IBOMA seems to be closer to the upper viscosity limit. In fact, reports on DLP printable composites indicate that the upper viscosity limit of the printable formulation is around 5 Pa·s [38,39]. Therefore, just samples C to F are considered suitable for DLP printing.

3.1.2. Study of the photocured materials

The photocured samples were evaluated by DMTA in order to assess the influence of IBOMA reactive diluent on the thermal and viscoelastic properties. Storage (E′) and tan δ curve (tan δ = E″/E′, where E″ is the loss modulus) were evaluated as function of temperature and plotted in Fig. 1d and e. Also, the corresponding glass transition temperature (T_g), defined as the peak of the tan δ curve, were evaluated. The apparent crosslinking density (ν_c), calculated according to Equation (3), and T_g values are summarized in Table 2.

It is observed that all curves present similar shape, characterized by a decrease in E′ with increasing temperature, indicating the transition between glass and rubbery states, i.e. the glass transition [40]. In the case of AESO, E′ decreases from 0.8 × 10^9 Pa to 3.0 × 10^7 Pa, while for sample F, containing 50 wt% of IBOMA, E′ changes from 1.2 × 10^9 Pa to 3.4 × 10^6 Pa. Thus, by increasing IBOMA content in the photocurable formulations, we could observe that the moduli in the glass state is maintaining almost constant while the moduli in the rubbery plateau decreases of 1 order of magnitude. The E′ in the rubbery plateau can be related to the crosslinking density (ν_c) and the obtained values of ν_c indicate a decrease of the crosslinking density when IBOMA content increases (from 2.84 down to 0.33 mmol/cm^3). This is ascribed to the fact that a monofunctional reactive diluent has been added to the photopolymerization system with a consequent decrease of the crosslinking density [41]. Therefore, when IBOMA molecules react in the photopolymerization process, the conversion of the double bonds can occur faster because of the mobility of the polymer chains (that is possible due to the lower viscosity of the material), agreeing with the results obtained for the photopolymerization process [42].

Interestingly, the addition of IBOMA to the AESO polymer, despite reducing the crosslinking density, induced an increase of the T_g of the photocured material, identified by the sharp increase of the maximum of the tan δ curves toward higher temperatures, from 38ºC of AESO pristine material to 107ºC for the sample containing 50 wt% of IBOMA reactive diluent. However, attending to the detail of the tan δ curves for the samples containing IBOMA, two domains of relaxation are detected: one slightly lower to the T_g of AESO pristine polymer network and almost constant for all samples, and second one at higher temperatures that increases in temperature with increasing IBOMA content. This can be attributed to a bi-phasic polymer network in which the IBOMA acts firstly as reactive diluent, reacting with the AESO molecule, and secondly generating free poly(IBOMA). When IBOMA molecule reacts with AESO, it does as chain ends into the crosslinked network which will reduce the T_g of the AESO material (as it is observed in the first relaxation), while when IBOMA homopolymerize it generates a second phase, a IBOMA-rich phase and/or free poly(IBOMA), which can present a T_g as high as 110 °C, according to [43]. Further, the intensity of the second peak observed in tan δ is higher when the IBOMA content increases. This fact can be associated with chains which are not strongly attached to the network and that hence can freely relax [44]. An schematic representation of the photocurable mechanism of the AESO:IBOMA resin is presented in Fig. 1f.

Table 2
Main properties of the AESO:IBOMA formulations and photocured samples.

Sample	t_{gel} (s)	ΔG′/Δt (kPa/s)	FTIR conversion (%)	Viscosity at shear rate of 10 s^{-1} (Pa·s)	T_g (ºC)	E'_R (MPa)	ν_c (mmol/cm^3)
A	2.5 ± 1.3	44.5 ± 1.1	77 ± 1	18.2 ± 1.1	38	30	2.84
B	1.6 ± 0.9	44.5 ± 1.2	79 ± 2	7.68 ± 0.02	50	25	2.37
C	1.3 ± 0.6	46.8 ± 0.7	74 ± 2	3.16 ± 0.05	57	20	1.90
D	1.2 ± 0.2	48.0 ± 1.3	76 ± 3	1.42 ± 0.03	76	16	1.52
E	2.6 ± 1.1	50.1 ± 2.4	75 ± 1	0.56 ± 0.01	92	4.1	0.39
F	2.5 ± 1.8	54.3 ± 1.6	77 ± 1	0.28 ± 0.01	107	3.5	0.33

3.2. Optimization of the electrically conductive composites

3.2.1. Characterization of the composite photocured formulations

Once the different formulations were prepared and characterized, three of them were selected based on their different characteristics and good capabilities for being printed by DLP. Multiwalled carbon nanotubes (MWCNT) are characterized by large aspect ratio, high electrical conductivity and mechanical reinforcing properties within polymers that make them the most used carbonaceous material for the preparation of conductive and sensing composites [45,46]. Thus, different contents of MWCNT were dispersed in the three selected formulations and composites were obtained and characterized.

First, the photopolymerization processability of the different composite formulations was evaluated using a real-time photorheology, following the same procedure explained in the section before. Here, similar curves as for the pristine formulations are obtained and the final values of $\Delta G'/\Delta t$ and t_{gel} for all composite materials are presented in Fig. 2a.

It is found that the addition of MWCNT to the formulations induced an increase on the t_{gel} and a decrease on the photopolymerization rate, independently on the diluent content. The t_{gel} of sample C increases approximately 5 times from 1.2 ± 0.2 s to 8.3 ± 1.5 s when just 0.2 wt% MWCNT content is added and increases even more when MWCNT content further increases, being as high as 29.3 ± 7.5 s in the case of 0.6 wt% MWCNT sample. Similar behaviour is obtained for the rest of the samples with the interesting fact that the lowest viscous formulation, the one containing 50 wt% of IBOMA reactive diluent (sample F), presents the lowest increase of t_{gel} when similar MWCTN content is added, being here 14.3 ± 2.1 s for 0.6 wt% MWCNT sample content. In addition, $\Delta G'/\Delta t$ is affected by the addition of MWCNT in a similar way for all formulations independently on the reactive diluent content. The $\Delta G'/\Delta t$ decreases more than a half in the case of sample D from 47.1 ± 3.2 kPa/s for the pristine sample to 18.1 ± 3.0 kPa/s when 0.2 wt% MWCNT is added. This decrease is even more pronounced when 0.6 wt% MWCNT content is added, leading to a final value of 2.3 ± 0.1 kPa/s. At this point, and in agreement with t_{gel} results, the curing rate values obtained for sample F are the highest among all photocurable formulations prepared, showing a value of 2.9 ± 0.4 kPa/s.

The negative effect of MWCNT over the UV curing can be ascribed to the UV shielding phenomena of the conductive carbonaceous material. MWCNT light absorption hinder the efficiency of the photoinitiator, delaying and slowing the photopolymerization of the filled formulations [34]. When the filler content increases, this unfavourable effect is even more pronounced and it is also magnified by the increase of viscosity [15]. Thus, when the viscosity of the initial pristine formulation is lower, the addition of the MWCNT affect in a lesser extent the photopolymerization process, together with the fact that formulation containing 50 wt% IBOMA is more reactive than the C formulation.

Attending to the FTIR results (Fig. 2b), the presence of MWCNT affects the conversion of double bonds, decreasing the total percentage of conversion when carbonaceous filler content increases, independently on the formulation investigated. The total conversion obtained decreases from approximately 77% in the pristine sample down to 67% for the composites presenting C base formulation and 0.6 wt% MWCNT or even close to 50% when F base formulation is used for the same filler content. These results are in agreement with the photorheology data and are explained by the light absorption of MWCNTs [15], as reported for other carbonaceous fillers incorporated into AESO polymer [31].

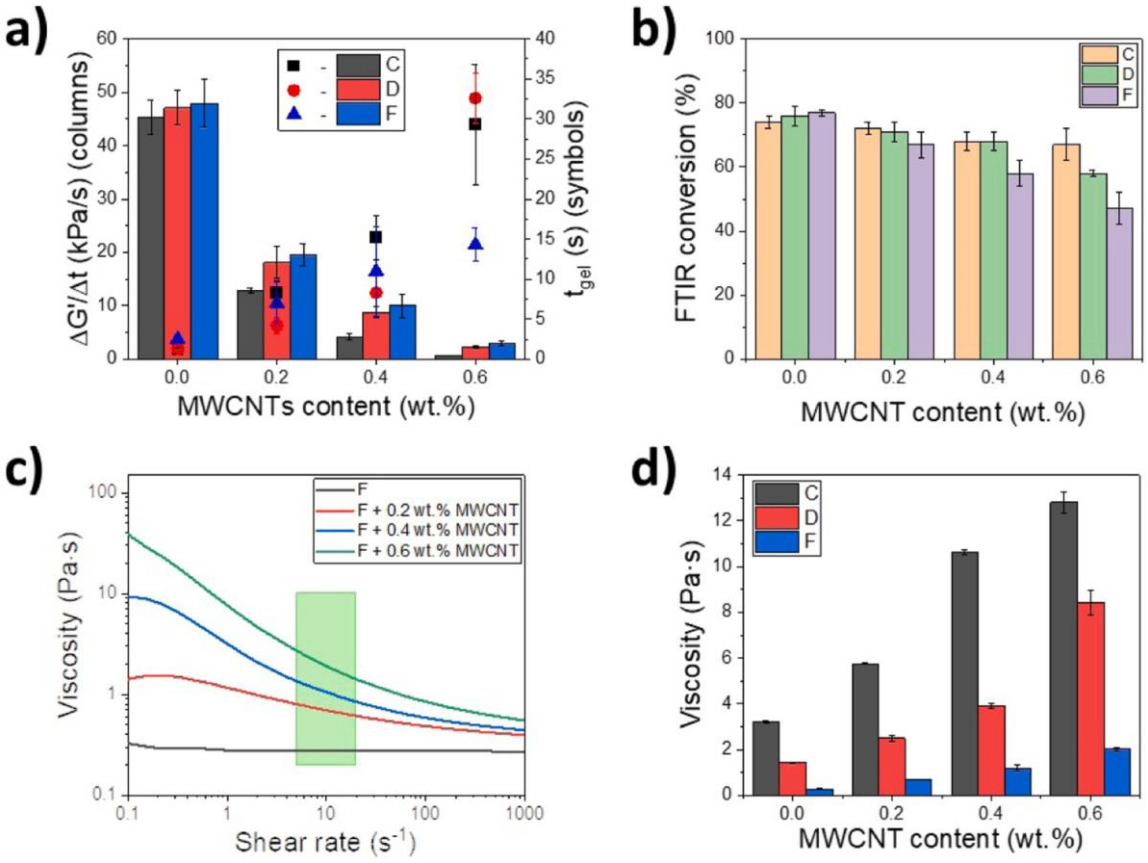

Fig. 2. a) Comparison of photopolymerization rate ($\Delta G'/\Delta t$) –columns- and gel time (t_{gel}) –symbols- for formulations C, D and F with different MWCNT contents. b) Comparison of FTIR double bond conversions for the same samples. c) Viscosity curves of the F formulation and its composites with MWCNT as a function of shear rate. The area in green represents the viscosity range recommended for DLP inks and the estimated range of shearing during printing. d) Comparison of viscosity values at shear rate of 10 $s^{-1}$for formulations C, D and F with different MWCNT contents.

Regarding viscosity results, the addition of MWNT increased the viscosity of the suspensions, especially at low shear rates, as presented in Fig. 2c. When MWCNT content increases, the viscosity increases in the whole shear rate range studied. Furthermore, the rheological behaviour of the formulations changed from Newtonian fluid to a non-Newtonian fluid with different viscosity at different shear rates [47]. Particularly, the formulations showed a shear thinning behaviour since the viscosity decreases when the shear rate increases as it has been observed in other MWCNT/polymer formulations [48]. This effect has been ascribed to the increasing interactions between the oligomeric chains and the nano-fillers [49].

In order to compare the different formulations and following the same procedure than for the pristine formulations (Section 3.1. Optimization of the polymer matrix), the viscosity values at a fixed shear rate of 10 are summarized in Table 2. When C formulation is employed, the addition of 0.2 wt% MWCNT doubles the viscosity values from 3.21 ± 0.07 Pa·s to 5.76 ± 0.04 Pa·s and increases almost 4 times when 0.6 wt% content is used to a final value of 12.80 ± 0.45 Pa·s. A similar behaviour is observed for the other formulations D and F but with a lower viscosity values when a 0.6 wt% MWCNT content is used, being 8.44 ± 0.54 Pa·s and 2.01 ± 0.08 Pa·s, respectively. Thus, considering the afore mentioned viscosity range for the printability of DLP composite formulations (maximum of 5 Pa·s) [38,39], C formulations containing 0.4 and 0.6 wt% MWCNT. together with the D formulation containing 0.6 wt% MWCNT, can be dismissed as usable formulations. Further, sample C containing 0.2 wt% MWCNT can be considered as a highly difficult printable material due to its viscosity close to the limit. In this sense, just F composite formulations and D material containing 0.4 wt% MWCNT can be exploitable for 3D printing.

3.2.2. Characterization of photocured composite samples

Photocured films similar to the one presented in Fig. 3a were obtained and cut with a rectangular shape and dimensions of 20 × 7.5 × 0.25 mm^3 for characterization. SEM, DMTA and electrical conductivity tests were used in order to characterized the MWCNT dispersion and to evaluate how the MWCNT affects the dynamic mechanical properties and the electrical conductivity of the samples.

The filler dispersion and wettability between MWCNT and the AESO: IBOMA polymer matrices are evaluated by the SEM images, the filler being identified as white dots and tubes [15]. Fig. 3b shows, as representative image for the rest of samples, the MWCNT dispersion within sample D containing 0.4 wt% MWCNT. For carbonaceous based composites, a suitable dispersion of the fillers is desirable as it has been demonstrated that the electrical conductivity of composites depends on MWCNT distribution within the polymer matrix [15]. Here, it is observed that MWCNTs are well dispersed along the material and that the polymer fully surrounds the fillers, not showing any voids or loose interfaces. Further, just a few small aggregates of several micrometres in diameter are observed, and those aggregates are well distributed within the polymer. In addition, it was demonstrated that a proper distribution of small agglomerates or clusters is more important than a good dispersion of individual fillers and can be beneficious to achieve higher electrical conductivity [50,51]. However, agglomerate distribution could affect other properties of composites, as is the case of the mechanical properties [50].

When filler content increases, the presence of white spots in the SEM images increases (Fig. S1 *of* Supporting Information), indicating the successful addition of higher MWCNT quantities. Particularly, when a 0.6 wt% MWCNT content is added, the viscosity of the different matrices promotes a different filler dispersion, being MWCNT better dispersed

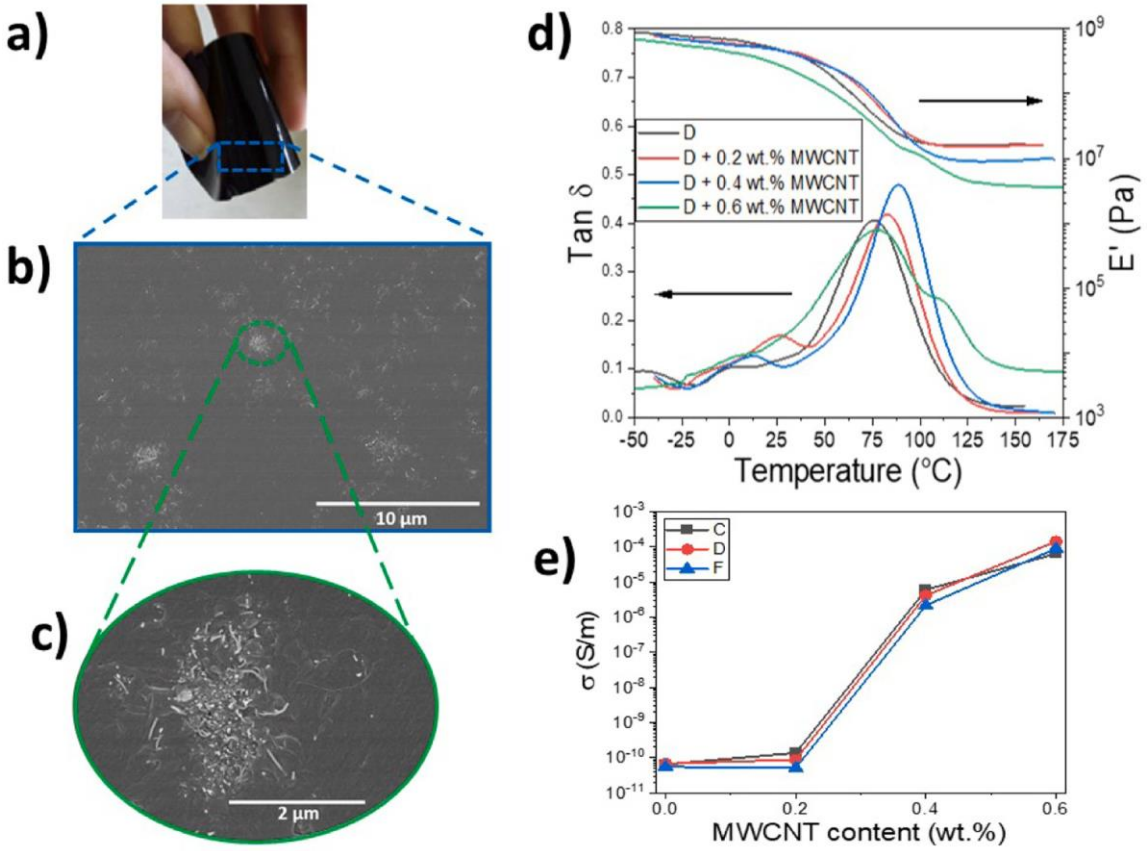

Fig. 3. a) Image of a photocured composite film obtained from sample D containing 0.4 wt% MWCNT. b) Representative SEM image of the same sample at magnification of 5000 × and c) of 20000 × . d) DMTA plots of photocured sample D and its composites. e) Electrical conductivity as a function of MWCNT content for all prepared composites up to 0.6 wt% filler content.

when less viscous polymer matrix is used. This is a typical behaviour for photocurable composites as it is reported in the literature [15,52].

The rectangular shape samples are then employed to characterized the dynamic mechanical properties of the prepared composites. As it can be observed in Fig. 3d for composites based on the polymer matrix D, the presence of MWCNT apparently does not affect the thermomechanical behaviour of the AESO:IBOMA material, presenting in all cases a single transition between the glassy and rubbery states (glass transition). The values of the E' at the rubbery plateau can be correlated with the ν_c as indicated in Eq. (3). Here, the presence of MWCNT induce a decrease of E'_R and hence in ν_c, whose values are indicated in Table 3. Thus, ν_c decrease from 1.90 to 1.65 mmol/cm^3 when 0.6 wt% MWCNT content is added to C sample. Similarly, sample D shows a decrease of ν_c from 1.52 to 0.36 mmol/cm^3 at the maximum filler content and sample F presents the lowest ν_c values that change between 0.33 and 0.015 mmol/cm^3 depending the MWCNT content.

The presence of MWCNT affects the photopolymerization process and the polymerization reaction due to the shielding effect of carbonaceous filler, as previously discussed. The reaction is slower and it occurs in a lesser extent, as photorheology results reveal (Fig. 2). This can cause that during the initiation step, less initiation points are reacted and, therefore, the crosslinking density decreases [31,52]. This is also confirmed by FTIR results, where it is observed that the double bond conversion decreases when MWCNT content increases. Furthermore, the same trend is observed independently on the polymer matrix employed and the obtained ν_c values are in correlation with the DMA results of the neat polymer matrices (the higher the content of monofunctional reac- tive diluent, the lower the crosslinking density).

Attending to the tan δ peak, its position and height are indicative of the structure and viscoelastic properties of a particular composite material. The presence of nanofillers, and particularly the MWCNT used in this work, can change the polymer chain mobility and deformability, being reflected in the behaviour of tan δ [53]. In the present case, for MWCNT content up to 0.4 wt%, the tan δ peak value shifts towards higher temperatures, indicating an increase of T_g from 76ºC to 87ºC for samples based on the polymer matrix D and an increase of the same order for the rest of polymer matrices. This can be attributed to the hindering of the polymeric chain mobility in the presence of the nanofiller. When the highest filler content is added, the large number of MWCNT agglomerates act as defects on the composite and can deteriorate the thermos-mechanical properties of the composites, with a decrease of the T_g of the final crosslinked material [15,52]. However, when the less viscous matrix is employed, the MWCNT dispersions is better as revealed the SEM images and T_g continuously increases in all filler content range studied.

The T_g of MWCNT/polymer composites depends on the interaction between the MWCNT and the polymer matrix. If the adhesion between filler and matrix is poor, free volumes inside the polymer matrix will be generated and consequently the T_g will be decreased. In contrast, if adhesion between MWCNT and polymer is good, the MWCNT can constraint the polymer chain mobility and can increase the T_g of com- posite material [54,55]. In this way, AESO:IBOMA matrix allows a good MWCNT dispersion when filler contents are below a critical value of 0.4 wt% as it is observed by the increase of T_g for all studied sample. However, for filler contents above that, polymer matrices that present high AESO content, i.e. the more viscous materials, cannot ensure good filler dispersion, as SEM results corroborate, and consequently, the T_g is decreased. Therefore, the AESO:IBOMA matrix presenting 50 wt% content of both components is the only matrix that demonstrates to be able to ensure good MWCNT dispersion in the all the filler content range studied.

Finally, the electrical conductivity (σ) of the prepared composites is characterized. The voltage/current (I-V) curves are measured applying voltages between — 10 to + 10 V and σ is obtained using the Eq. (4). Table 3 shows the σ values for all samples and Fig. 3e depicts the evolution of σ as a function of MWCNT content for the different polymer matrices.

The electrical conductivity of the pristine polymer samples is in the order of 7 × 10^{-11} S/m, characterizing insulator materials. The addition of 0.2 wt% MWCNT, does not lead to a significantly variation of σ (less than 1 order of magnitude), whereas for 0.4 wt% filler content, an increase of 5 orders in magnitude can be appreciated independently on the polymer matrix. Moreover, samples containing the highest filler content presented the highest σ values that are close to 1 × 10^{-4} S/m. This sharp increase of σ in several orders of magnitude corresponds to a percolative system [56]. However, attending to the shape of the curves and considering the results obtained for other photocured MWCNT/polymer composites [15,57], it seems that σ could eventually increase even more in case samples could be actually photocured, so the actual percolation threshold is difficult to be elucidated.

Table 3
Main evaluated physical-chemical and functional properties of formulations and photocured samples of AESO:IBOMA and their composites with MWCNT.

Sample	MWCNT content (wt%)	t_{gel} (s)	ΔG'/Δt (kPa/s)	FTIR conversion (%)	Viscosity at shear rate of 10 s^{-1} (Pa·s)	T_g (ºC)	E'_R (MPa)	ν_c (mmol/cm^3)	Conductivity (S/m)
C	0	1.2							± 2.1
	0.2	± 0.2 8.3							
	0.4	± 1.5 15.2							
	0.6	± 2.8 29.3							
D	0	± 7.5 1.3							
	0.2	± 0.3 4.2							
	0.4	± 1.0 8.3							
	0.6	± 0.6 32.6							
F	0	± 3.2 2.5							
	0.2	± 0.5 7.0							
	0.4	± 2.6 11.0							
	0.6	± 5.6 14.3							

43.3 ± 3.3	74 ± 2 3.21 ± 0.07 57 20 1.90 6.5 × 10^{-11}		6.0 × 10^{-6}					
		0.7 ± 0.1	67 ± 5	12.80 ± 0.45	63	15	1.65	6.4 × 10^{-5}
		47.1 ± 3.2	76 ± 3	1.43 ± 0.04	76	16	1.52	6.8 × 10^{-11}
		18.1 ± 3.0	71 ± 3	2.49 ± 0.12	81	15	1.49	8.8 × 10^{-11}
12.8 ± 0.5	72 ± 2 5.76 ± 0.04 61 19 1.88 1.4 × 10^{-10}	8.8 ± 1.0	68 ± 3	3.93 ± 0.10	87	9.2	0.87	4.1 × 10^{-6}
		2.3 ± 0.1	58 ± 1	8.44 ± 0.54	76	3.8	0.36	1.4 × 10^{-4}
		47.9 ± 4.5	77 ± 1	0.28 ± 0.01	107	3.5	0.33	5.5 × 10^{-11}
4.2 ± 0.6	68 ± 3 10.63 ± 0.09 66 17 1.81	19.5 ± 2.1	67 ± 4	0.68 ± 0.01	110	0.25	0.022	5.2 × 10^{-11}
		10.0 ± 2.2	58 ± 4	1.19 ± 0.12	120	0.22	0.020	2.1 × 10^{-6}
		2.9 ± 0.4	47 ± 5	2.01 ± 0.08	123	0.17	0.015	8.9 × 10^{-5}

In the present case, the maximum amount of MWCNT allowed compatible with UV curing and viscoelastic properties has been added, so the obtained electrical conductivity is the maximum allowed for this MWCNT/AESO:IBOMA system. Interestingly, the σ values at a fixed MWCNT content apparently is not influenced by the viscoelastic properties of the polymer matrix. Thus, all samples presenting 0.6 wt% MWCNT content are similar in terms of electrical conductivity. However, considering the afore explained viscoelastic properties of photocured materials and the better processability in terms of photopolymerization and viscosity of the composite formulations, the sample containing 0.6 wt% MWCNT and AESO:IBOMA polymer matrix in 50:50 ratio is the best candidate to obtain 3D printable electrically conductive polymer composites.

3.3. 3D printing of functional composites

Once the optimal formulation has been selected, its processability through digital light processing (DLP) printing and the different functional properties of the printed parts are characterized. As it is concluded in the previous section, the formulation presenting 0.6 wt% MWCNT content and 50:50 wt% AESO:IBOMA polymer matrix is selected as being the most suitable formulation for 3D printing of electrically conductive composites.

First, the printability by DLP of the sample containing 0.6 wt% MWCNT and AESO:IBOMA (50:50) polymer matrix, named merely as formulation hereafter, is tested. Considering the viscosity and photorheology results previously discussed, printing parameters are adjusted in order to be able to cure formulation during the printing process and to attach it to the printing platform without presenting over cure. As the viscosity of the formulation is around 2 Pa·s, the working temperature for the 3D printer is slightly increased from room temperature to 40ºC and the approach velocity of the platform is reduced to the minimum (1.5 mm/s) in order to facilitate the movement of the formulation during the layer-by-layer process. Other important parameters as exposure time and light intensity were also adjusted to obtain the highest printed sample quality in the shorter time. In this sense, an exposure time of 8 s, a light intensity of 35 mW/cm^2 and layer thickness of 50 μm are the parameters used. Thus, considering all the printing parameters for this formulation, the 3D printing throughput is around 3 mm/h.

In order to evaluate the resolution and the capabilities of the

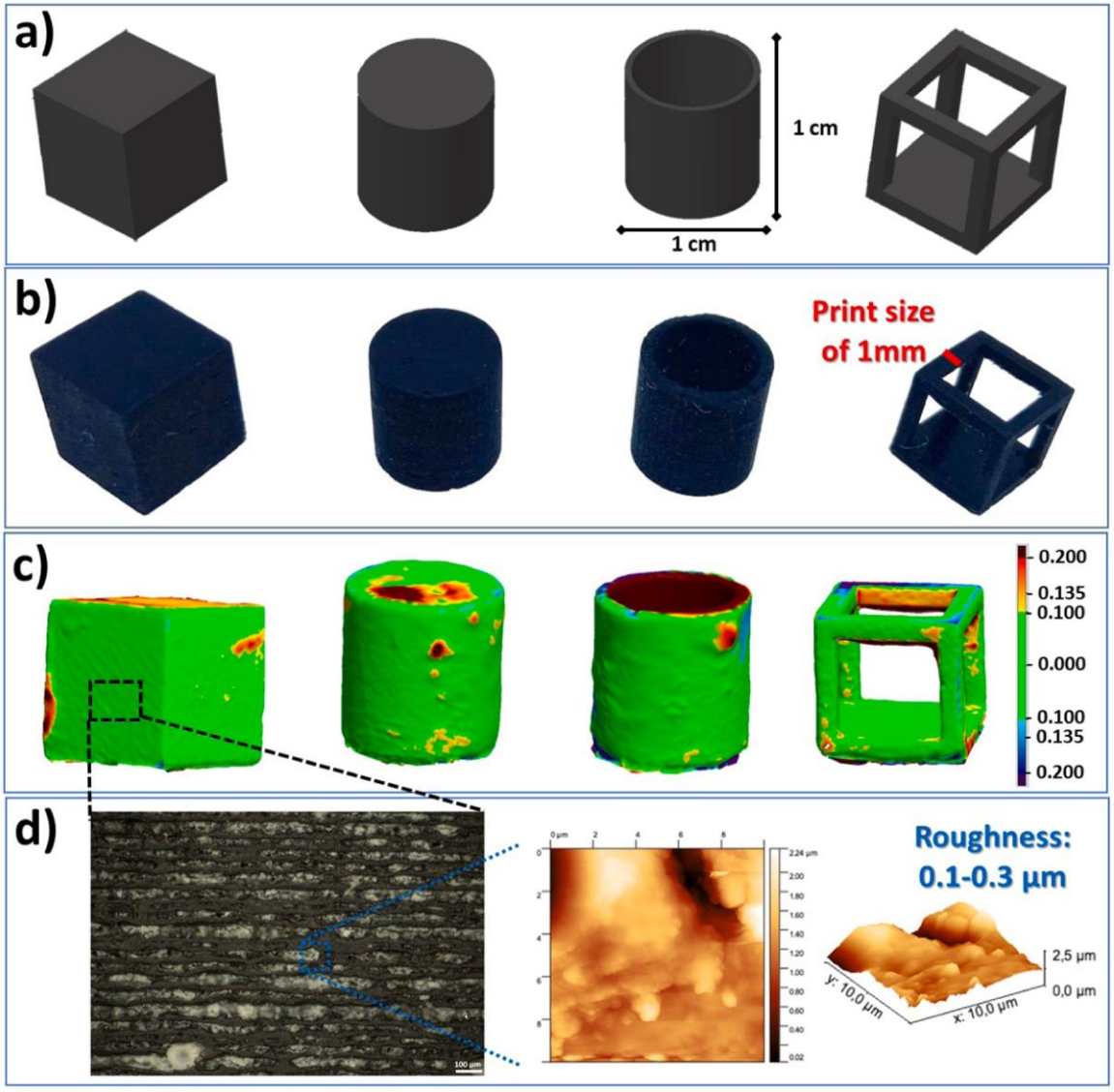

Fig. 4. a) CAD models for DLP printing of filled cube and cylinder, and hollow cylinder and cube. b) Photographs of the printed objects. c) 3D image obtained with the 3D scanner with the evaluation of the variations between the CAD project and the printed object. d) Analysis of the roughness: in the left the microscope image of filled cube face and in the right the AFM analysis of the same sample.

formulation to be 3D printed by DLP, different shapes are printed. On the one hand, simple parts presenting different types of edges are printed: a filled cube presenting flat surfaces and straight elements and a filled cylinder with rounded surfaces. Further, more complex structures presenting hollows, thin elements and overhangs are printed: a hollow cylinder and a hollow cube. All digital CAD models are depicted in Fig. 4a while the real images of the 3D printed objects are presented in Fig. 4b. It is observed that despite the high formulation viscosity and the strong light absorption by the MWCNT, all four samples are able to be 3D-printed with a good appearance. In the case of cubic samples (both filled and hollow cubes), the printed objects are characterized by flat surfaces, straight elements, and clean and sharp edges while both cylinders present good smooth rounded surface and accurate dimensions.

Then, to evaluate the precision of the printing process, that is, to measure the shape fidelity of the printed object to the reference CAD [58], a 3D scan of the samples is carried out. In this sense, the accuracy was proved by performing a comparison between the digital file and the scan of 3D printed object. This generates a three-dimensional model that presents an overlap heat map displaying the deviation between both the digital file and the scan of each printed sample, as represented in Fig. 4c. It results in an average variation from the CAD virtual project of around ± 0.100 mm in the green zones and ± 0.135 mm in the yellow and light blue ones, indicating a good fabrication precision [18]. Particularly, in the case of both filled samples, some surface roughness can be appreciated at top parts and also at specific points of the lateral walls. This irregularities and divergences can be attributed to several factors, such as the printer resolution or printing errors, in addition to an irregular distribution of the talcum powder on the surface of the objects, which is used to improve scanning efficiency [58]. Regarding to the hollow structures, both cylinder and cube present the same good printing quality mentioned before and some irregularities at the hollow parts or at overhangs in the case of the cube. This can be ascribed to the same reasons explained, in addition to scanner precision and its difficulty to properly detect internal areas of the structures.

In order to analyze the surface roughness of the 3D printed materials, initially, optical photographs have been obtained at the surface of the filled cube. Fig. 4d shows a representative image of the sample in which the disposition of the different successive layers obtained during the 3D printing process can be observed. Considering the scale, the thickness of each layer is demonstrated to be around 45–55 μm, which is in correlation with the layer height set to the printer during the printing process and what confirms that the printing process went well. However, as can be observed in the image, some defects were presented in form of small balls or cuts along some layer which was also observed by SEM analysis of the printed parts (see below) and that can be related to MWCNT agglomerations. The analysis of the profilometry allows to characterize how is the surface quality (by means of roughness) of the printed materials. Thus, surface roughness of around 4.5 μm was obtained indicating a good surface finish despite the defects observed by microscopy.

Going in deep with this analysis, AFM measurements allows the characterization of surface roughness at a lower level. Regarding to this analysis, five 10 × 10 μm^2 images were obtained at five different locations on one of the faces of the cube, two at each corner of the face and one in the middle. The 2D and 3D topography images of one of the scanned areas are presented in Fig. 4d.

With this, we obtained a value for the roughness of R_q = 219 ± 113 nm (around 0.1–0.3 μm), indicating a good quality of the surface finish. Considering the surface dimensions analyzed, the 3D map obtained and the results obtained by microscopy images and profilometry, this roughness can be related with the same defects explained before

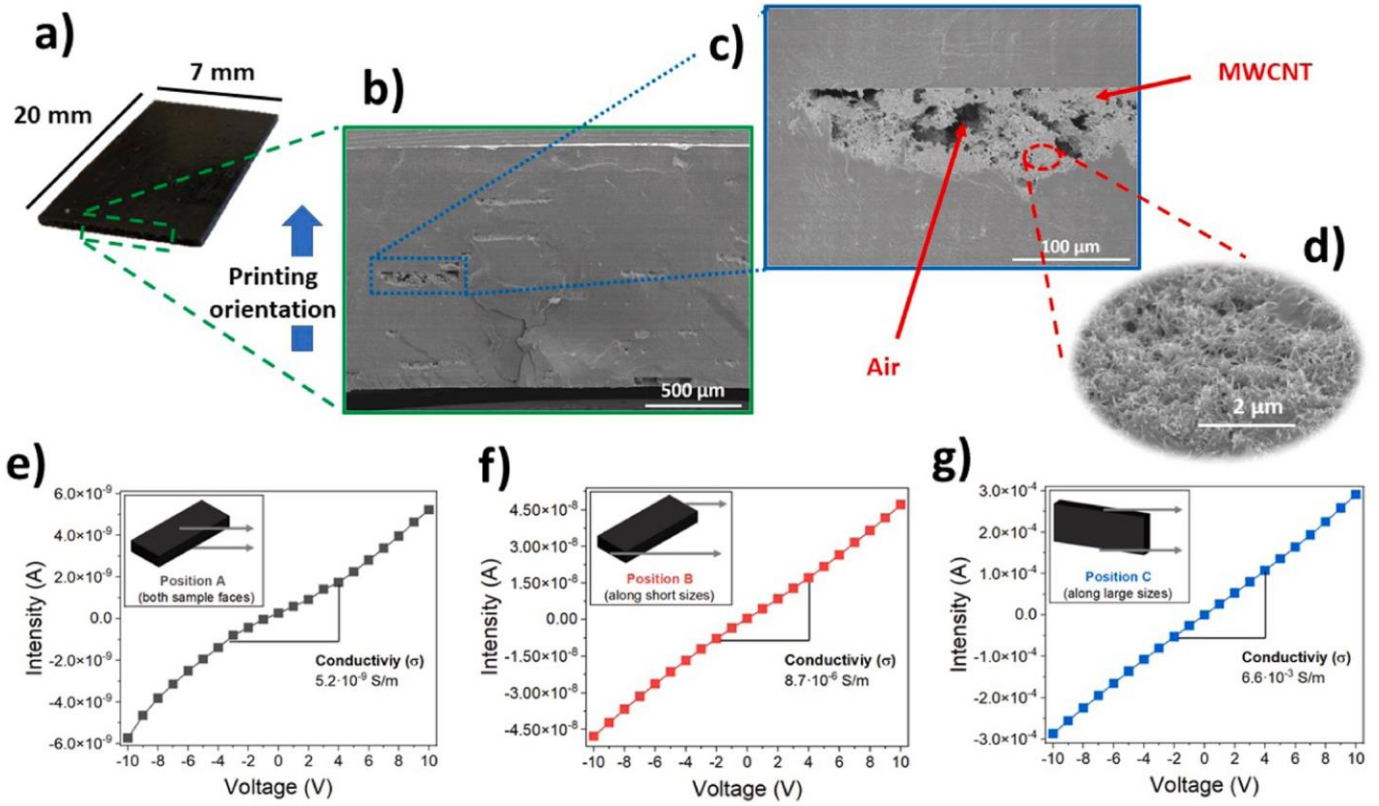

Fig. 5. a) Rectangular shape 3D printed sample obtained with dimensions of 20 × 7.0 × 1.5 mm^3. b) SEM image of the cross-section of the printed part obtained at magnification of 60 × . c) SEM image of one characteristic MWCNT agglomerations obtained at magnification of 400 × . d) SEM image of MWCNT presented in the 3D printed sample obtained at magnification of 20000 × . From e) to g), voltage/current (I-V) curves obtained with the corresponding electrical conductivity (σ) value for each electrode position (measurement orientation).

ascribed to MWCNT agglomeration.

When good printability has been confirmed, functional samples are 3D printed using the same conditions previously detailed. For an easy data processing and clear understanding of the electrical conductivity, rectangular shape samples are printed with dimensions of 20 × 7.0 × 1.5 mm^3 (Fig. 5a). It is to be noticed that the thickness is higher compared with the photocured samples employed in the previous characterization, fact that is possible because DLP printing is a layer-by-layer process in which thin layers of 50 μm are cured. Further, light can pass through the entire thickness and be easily absorbed by the material along the whole thickness.

MWCNT dispersion within the 3D printed samples as well as electrical conductivity through the printed parts at different orientations is evaluated in order to detect possible internal imperfections or MWCNT agglomerations occurring during the printing process. As can be seen in the SEM images presented in Fig. 5b to d, MWCNTs can be identified as white spots and tubes along the materials. The cross-section image of the whole rectangular sample (Fig. 5b) shows different agglomeration areas that present both MWCNT aggregates and voids, better observed in the magnified images of Fig. 5c and d. It needs to be noticed that these agglomerations present one quasi-perfect linear edge perpendicular to the printing direction (i.e. parallel to each layer of the printed object) and thickness closed to 50 μm. This fact can be ascribed to specific MWCNT agglomerations that occur during the illumination of one layer that, after the photocuring process and the subsequently movement of the building platform, new liquid material is placed between the cured layer and thereafter the MWCNT agglomeration is moved or transferred to another point of the object. This could also explain why more MWCNT agglomerations with square shape and 50 μm thickness can be observed at other points of the 3D printed object and at different heights.

Nevertheless, the printed objects presented good quality and MWCNT can be identified along all the rectangular printed material. Further, it is demonstrated that good distribution of filler agglomerations does not hinder significantly the mechanical properties and that a good distribution of agglomerates or clusters allows achieving higher electrical conductivity that individual filler dispersion [50,51].

After the filler dispersion of the printed samples were characterized, the influence of printing process on the electrical conductivity, σ, was studied. As it is demonstrated in the literature, the printing parameters such as printing orientation or printing infill density can change σ values in several orders of magnitude [59–61]. Thus, in this work, three different electrode positions were employed: position A, in which electrodes are placed in both faces of the rectangular sample, position B in which electrodes are placed in the shorter dimensions of the rectangle and position C where the electrodes are placed in the larger dimensions (Fig. 5e to g insets, respectively).

Fig. 5e to g show that the σ values of the printed material depends on the electrodes position. When electrodes are placed in position A (both sample faces), the σ obtained is 5.2 × 10^{-9} S/m, while position B (along short sizes) presents a σ value of 8.7 × 10^{-6} S/m and the highest conductivity is achieved when position C (along large sizes) are used with an σ value of 6.6 × 10^{-3} S/m. These differences of almost 3 orders of magnitude between all them can be explained in terms of the printing process and the quality of filler dispersion. Previously shown SEM images indicate that MWCNT agglomeration occurs at different points of the sample along the cross-section in form of small squares that present both MWCNT aggregates and voids. When electrical current is tried to be passed through the sample from one face to another, these micrometric pores act as insulator points and electrical conductivity compatible with an electrical conductor is not achieved. However, when current is applied at the edges of the sample (positions B and C), the whole sample can present a continuous electrical path for electrical current and σ values obtained in these orientations are higher.

Regarding to the differences observed between positions B and C, it needs to be noticed two main factors. The first one is the electrodes distance. When position B is used, the distance through the electrical current needs to pass is higher than in position C. By increasing the distance, we can have an enhancement of void defects probability along the path, leading to a decrease of the electrical conductivity. The second one is the possible MWCNT orientation that could occur during the printing process [62]. The building platform has a rectangular shape in which the long side of the rectangle is parallel to the movement of the blade that spreads the resin between the different printed layers. Thus, the 3d printing process undergoes by the following steps: firstly, the platform goes down inside the vat with the resin, and the doctor blade or squeegee that is located under the vat is moved making some pressure between the bottom part of the FEP of the vat, the resin and the platform that is inside the resin and at a distance to the FEP of 50 μm. This spreads the resin in a uniform layer. This movement can mechanically orientate the MWCNT. Then, UV light is switched on during 8 s and the layer of 50 μm is cured and attached to the platform (or to the previous layer in case of the rest of the layers except to the initial one). Then, the platform moves up and subsequently down leaving the resin to enter between the cured layer attached to the platform and the FEP. Then, the blade moves to spread again the resin to have a uniform layer of liquid resin (similar procedure explained above). During this movement, the MWCNT are again oriented in the same direction as the blade always moves from front to back making pressure and spreading the liquid resin of the vat. Therefore, layer by layer, the MWCNT are mechanically oriented by the movement of the blade and the material photocured by UV light irradiation, "freezing" thus the oriented MWCNT in the 3D cured structure and generating a preferential orientation of MWCNT along the vat. In this sense, MWCNT could create a preferential direction for electrical conductivity and an electrical conductivity anisotropy for 3D printed composite samples. Therefore, considering the placement direction in which the rectangle samples are cured in the platform, this orientation of the MWCNT are consistent with the higher electrical conductivity measured for the position C than position B.

Throughout, it can be concluded that functional composite materials based on bio-renewable polymer matrix and carbon nanotubes are obtained presenting good printability and electrical conductivity anisotropy.

4. Conclusions

In this work, acrylated epoxidized soybean oil (AESO) has been successfully combined with isobornyl acrylate (IBOMA) as reactive diluent to obtain 3D printable formulations with different physicochemical properties. When higher contents of IBOMA are added, the viscosity of the photocurable formulation is reduced of two orders of magnitude from 18.2 ± 1.1–0.28 ± 0.01 Pa·s, whereas the photopolymerization rate (ΔG'/Δt) increased from 44.5 ± 1.1–54.3 ± 1.6 kPa/s. Advantageously, gel time (t_{gel}) is maintained in all cases at around 2 ± 1 s, as well as double bond conversion at 75%, with a bio- renewable carbon content of at least 77.7%. The addition of IBOMA demonstrated to generate a two-phasic polymeric network in which the IBOMA acts firstly as reactive diluent reacting together with the AESO molecule and secondly generating free poly(IBOMA), reducing the crosslinking density of the final material.

When multiwalled carbon nanotubes (MWCNT) are added to the photocurable formulations, t_{gel} is increased and ΔG'/Δt decreased independently on the IBOMA and filler contents. For higher MWCNT quantities (up to 0.6 wt%), both photocuring parameters are strongly affected and photopolymerization is hindered, with a final conversion that is reduced to a minimum around 50%. The viscosity in the printing shear rate range increases when MWCNT are added, being suitable for 3D printing only the samples containing AESO:IBOMA in 50:50 ratio. In addition, the MWCNT dispersion of the photocured films obtained from these formulations is characterized by well dispersed fillers along the material, not showing any voids or loose interfaces. For the highest filler content, a few small aggregates of several micrometres in diameter well distributed along the material are observed, which are beneficious to

achieve electrical conductivities that increases from 5.5 × 10^{-11} S/m in pristine material to 8.9 × 10^{-5} S/m for 0.6 wt% MWCNT content sample.

For the highest electrically conductive material (MWCNT/AESO: IBOMA 50:50 and 0.6 wt% filler content), the printability of the formulation was characterized by digital light processing 3D printing of complex bulk and hollow structures, obtaining good fabrication precision with quality accuracy of ± 0.1 mm and surface roughness around 0.1 – 0.3 µm. Analyzing the MWCNT dispersion within the 3D printed structure, isolated filler agglomerations together with voids were observed. These agglomerations were randomly dispersed on the 3D part.

Finally, anisotropic electrical conductivity was obtained with conductivity values that can change in almost 6 orders of magnitude depending on the orientation with respect the to the printing patterns, being 6.6·10^{-3} S/m when electrical conductivity is measured parallel to the printing orientation and 5.2·10^{-9} S/m for perpendicular orientation with respect to the printed pattern. These differences were explained in terms of printing process and quality of filler dispersion that, in the one hand, can made the MWCNT to gain a preferential orientation during processing and, in the other hand, due to MWCNT agglomerations that can act as defects for electrical conductivity.

In conclusion, electrically conducting functional composite materials based on bio-renewable polymer matrix and carbon nanotubes are obtained presenting good 3D printability and electrical conductivity anisotropy.

CRediT authorship contribution statement

Cristian Mendes-Felipe: Conceptualization, Data curation, Investigation, Methodology, Validation, Writing – original draft, Writing – review & editing. **Riccardo Cofano:** Investigation, Methodology, Formal analysis. **Ander Garcia:** Writing – review & editing, Writing – original draft, Investigation, Formal analysis. **Marco Sangermano:** Funding acquisition, Writing – review & editing, Project administration, Conceptualization. **Senentxu Lanceros-Mendez:** Writing – review & editing, Resources, Funding acquisition, Project administration, Conceptualization, Resources.

Declaration of Competing Interest

The authors declare that they have no known competing financial interests or personal relationships that could have appeared to influence the work reported in this paper.

Data Availability

No data was used for the research described in the article.

Acknowledgements

Financial support from the Basque Government Education (POS-E_2021_2_0001) and Industry (Elkartek program) Departments is acknowledged. This study forms part of the Advanced Materials pro- gram and was supported by MCIN with funding from European Union NextGenerationEU (PRTR-C17. I1) and by The Basque Government under the IKUR program. Technical and human support provided by SGIker (UPV/EHU, MICINN, GV/EJ, EGEF, and ESF) is gratefully acknowledged.

Appendix A. Supporting information

Supplementary data associated with this article can be found in the online version at doi:10.1016/j.addma.2023.103867.

References

[1] O. Okorie, K. Salonitis, F. Charnley, M. Moreno, C. Turner, A. Tiwari, Digitisation and the circular economy: a review of current research and future trends, Energies 11 (2018) 3009, https://doi.org/10.3390/en11113009.
[2] P. Pandit, G.T. Nadathur, S. Maiti, B. Regubalan, Functionality and properties of bio-based materials, in: A. Shakeel (Ed.), Bio-Based Mater. Food Packag. Green Sustain. Adv. Packag. Mater., First ed., Springer, 2018, pp. 81–104, https://doi.org/10.1007/978-981-13-1909-9_4.
[3] R.P. Babu, K. O'Connor, R. Seeram, Current progress on bio-based polymers and their future trends, Prog. Biomater. 2 (2013) 8, https://doi.org/10.1186/2194-0517-2-8.
[4] I. Laskurain-Iturbe, G. Arana-Landín, B. Landeta-Manzano, N. Uriarte-Gallastegi, Exploring the influence of industry 4.0 technologies on the circular economy, J. Clean. Prod. 321 (2021), 128944, https://doi.org/10.1016/j.jclepro.2021.128944.
[5] V.S.D. Voet, J. Guit, K. Loos, Sustainable photopolymers in 3D printing: a review on biobased, biodegradable, and recyclable alternatives, Macromol. Rapid Commun. 42 (2021), 2000475, https://doi.org/10.1002/marc.202000475.
[6] F. Zhang, L. Zhu, Z. Li, S. Wang, J. Shi, W. Tang, N. Li, J. Yang, The recent development of vat photopolymerization: a review, Addit. Manuf. 48 (2021), 102423, https://doi.org/10.1016/j.addma.2021.102423.
[7] E.M. Maines, M.K. Porwal, C.J. Ellison, T.M. Reineke, Sustainable advances in SLA/DLP 3D printing materials and processes, Green. Chem. 23 (2021) 6863–6897, https://doi.org/10.1039/d1gc01489g.
[8] S. Ford, M. Despeisse, Additive manufacturing and sustainability: an exploratory study of the advantages and challenges, J. Clean. Prod. 137 (2016) 1573–1587, https://doi.org/10.1016/j.jclepro.2016.04.150.
[9] M. Sangermano, N. Razza, J.V. Crivello, Cationic UV-curing: technology and applications, Macromol. Mater. Eng. 299 (2014) 775–793, https://doi.org/10.1002/mame.201300349.
[10] C. Mendes-Felipe, J. Oliveira, I. Etxebarria, J.L. Vilas-Vilela, S. Lanceros-Mendez, State-of-the-art and future challenges of UV curable polymer-based smart materials for printing technologies, Adv. Mater. Technol. 4 (2019), 1800618, https://doi.org/10.1002/admt.201800618.
[11] D.S. Branciforti, S. Lazzaroni, C. Milanese, M. Castiglioni, F. Auricchio, D. Pasini, D. Dondi, Visible light 3D printing with epoxidized vegetable oils, Addit. Manuf. 25 (2019) 317–324, https://doi.org/10.1016/j.addma.2018.11.020.
[12] Y. Luo, G. Le Fer, D. Dean, M.L. Becker, 3D printing of poly(propylene fumarate) oligomers: evaluation of resin viscosity, printing characteristics and mechanical properties, Biomacromolecules 20 (2019) 1699–1708, https://doi.org/10.1021/acs.biomac.9b00076.
[13] C. Vazquez-Martel, L. Becker, W.V. Liebig, P. Elsner, E. Blasco, Vegetable oils as sustainable inks for additive manufacturing: a comparative study, ACS Sustain. Chem. Eng. 9 (2021) 16840–16848, https://doi.org/10.1021/acssuschemeng.1c06784.
[14] E. Skliutas, M. Lebedevaite, S. Kasetaite, S. Rekˇstyteˇ, S. Lileikis, J. Ostrauskaite, M. Malinauskas, A bio-based resin for a multi-scale optical 3D printing, Sci. Rep. 10 (2020) 1–9, https://doi.org/10.1038/s41598-020-66618-1.
[15] C. Mendes-Felipe, J. Oliveira, P. Costa, L. Ruiz-Rubio, A. Iregui, A. Gonz´alez, J. L. Vilas, S. Lanceros-Mendez, Stimuli responsive UV cured polyurethane acrylated/carbon nanotube composites for piezoresistive sensing, Eur. Polym. J. 120 (2019), 109226, https://doi.org/10.1016/j.eurpolymj.2019.109226.
[16] G. Malucelli, A. Fioravanti, L. Francioso, C. De Pascali, M.A. Signore, M.C. Carotta, A. Bonanno, D. Duraccio, Preparation and characterization of UV-cured composite films containing ZnO nanostructures: effect of filler geometric features on piezoelectric response, Prog. Org. Coat. 109 (2017) 45–54, https://doi.org/10.1016/j.porgcoat.2017.04.020.
[17] C. Mendes-Felipe, M. Salado, L.C. Fernandes, D.M. Correia, L. Ruiz-Rubio, M. Tariq, J.M.S.S. Esperança, J.L. Vilas-Vilela, S. Lanceros-Mendez, Photocurable temperature activated humidity hybrid sensing materials for multifunctional coatings, Polym. (Guildf.) 221 (2021), 123635, https://doi.org/10.1016/j.polymer.2021.123635.
[18] M. Gastaldi, I. Roppolo, A. Chiappone, C. Garino, A. Fin, M. Manachino, P. Sirianni, G. Viscardi, L. Scaltrito, M. Zanetti, S. Bordiga, C. Barolo, Thermochromic photoluminescent 3D printed polymeric devices based on copper-iodide clusters, Addit. Manuf. 49 (2022), 102504, https://doi.org/10.1016/j.addma.2021.102504.
[19] S. Chen, Y. Song, D. Ding, Z. Ling, F. Xu, Flexible and anisotropic strain sensor based on carbonized crepe paper with aligned cellulose fibers, Adv. Funct. Mater. 28 (2018), 1802547, https://doi.org/10.1002/adfm.201802547.
[20] D. Song, M.J. Zeng, P. Min, X.Q. Jia, F.L. Gao, Z.Z. Yu, X. Li, Electrically conductive and highly compressible anisotropic MXene-wood sponges for multifunctional and integrated wearable devices, J. Mater. Sci. Technol. 144 (2023) 102–110, https://doi.org/10.1016/j.jmst.2022.09.050.
[21] T. Fan, Y.Y. Zhang, S.S. Xue, Y.Q. Li, P. Huang, N. Hu, K. Liao, S.Y. Fu, Heterogeneous carbon/silicone composite for ultrasensitive anisotropic strain sensor with loading-direction-perception capability, Compos. Sci. Technol. 227 (2022), 109565, https://doi.org/10.1016/j.compscitech.2022.109565.
[22] J. Chen, X. Liu, Y. Tian, W. Zhu, C. Yan, Y. Shi, L.B. Kong, H.J. Qi, K. Zhou, 3D-printed anisotropic polymer materials for functional applications, Adv. Mater. 34 (2022), 2102877, https://doi.org/10.1002/adma.202102877.
[23] K. Markandan, C.Q. Lai, Fabrication, properties and applications of polymer composites additively manufactured with filler alignment control: a review, Compos. Part B Eng. 256 (2023), 110661, https://doi.org/10.1016/j.compositesb.2023.110661.

[24] P.S. Goh, A.F. Ismail, B.C. Ng, Directional alignment of carbon nanotubes in polymer matrices: contemporary approaches and future advances, Compos. Part A Appl. Sci. Manuf. 56 (2014) 103–126, https://doi.org/10.1016/j.compositesa.2013.10.001.
[25] L. Lu, X. Tang, S. Hu, Y. Pan, Acoustic field-assisted particle patterning for smart polymer composite fabrication in stereolithography, 3D Print. Addit. Manuf. 5 (2018) 151–159, https://doi.org/10.1089/3dp.2017.0157.
[26] D.E. Yunus, S. Sohrabi, R. He, W. Shi, Y. Liu, Acoustic patterning for 3D embedded electrically conductive wire in stereolithography, J. Micromech. Microeng. 27 (2017), 045016, https://doi.org/10.1088/1361-6439/aa62b7.
[27] S. Ushiba, S. Shoji, K. Masui, P. Kuray, J. Kono, S. Kawata, 3D microfabrication of single-wall carbon nanotube/polymer composites by two-photon polymerization lithography, Carbon 59 (2013) 283–288, https://doi.org/10.1016/j.carbon.2013.03.020.
[28] W. Xiong, Y. Liu, L.J. Jiang, Y.S. Zhou, D.W. Li, L. Jiang, J.F. Silvain, Y.F. Lu, Laser-directed assembly of aligned carbon nanotubes in three dimensions for multifunctional device fabrication, Adv. Mater. 28 (2016) 2002–2009, https://doi.org/10.1002/adma.201505516.
[29] Y. Liu, W. Xiong, D.W. Li, Y. Lu, X. Huang, H. Liu, L.S. Fan, L. Jiang, J.F. Silvain, Y. F. Lu, Precise assembly and joining of silver nanowires in three dimensions for highly conductive composite structures, Int. J. Extrem. Manuf. 1 (2019), https://doi.org/10.1088/2631-7990/ab17f7.
[30] M. Lebedevaite, V. Talacka, J. Ostrauskaite, High biorenewable content acrylate photocurable resins for DLP 3D printing, J. Appl. Polym. Sci. 138 (2021), 50233, https://doi.org/10.1002/app.50233.
[31] C. Mendes-Felipe, P. Costa, I. Roppolo, M. Sangermano, S. Lanceros-Mendez, Bio-based piezo- and thermoresistive photocurable sensing materials from acrylated epoxidized soybean oil, Macromol. Mater. Eng. 307 (2022), 2100934, https://doi.org/10.1002/mame.202100934.
[32] C. No`e, L. Iannucci, S. Malburet, A. Graillot, M. Sangermano, S. Grassini, New UV-curable anticorrosion coatings from vegetable oils, Macromol. Mater. Eng. 306 (2021), 2100029, https://doi.org/10.1002/mame.202100029.
[33] R. Harikrishna, S.M. Bhosle, S. Ponrathnam, C.R. Rajan, Synthesis and photopolymerization kinetics of linear alicyclic urethane acrylate macromonomer in presence of reactive diluents, J. Mater. Sci. 46 (2011) 2221–2228, https://doi.org/10.1007/s10853-010-5060-9.
[34] A. Cort´es, A. Cosola, M. Sangermano, M. Campo, S. Gonza´lez Prolongo, C.F. Pirri, A. Jim´enez-Su´arez, A. Chiappone, DLP 4D-printing of remotely, modularly, and selectively controllable shape memory polymer nanocomposites embedding carbon nanotubes, Adv. Funct. Mater. 31 (2021), https://doi.org/10.1002/adfm.202106774.
[35] X. Li, D. Wang, L. Zhao, X. Hou, L. Liu, B. Feng, M. Li, P. Zheng, X. Zhao, S. Wei, UV LED curable epoxy soybean-oil-based waterborne PUA resin for wood coatings, Prog. Org. Coat. 151 (2021), 105942, https://doi.org/10.1016/j.porgcoat.2020.105942.
[36] T. Kuhnt, F.L.C. Morgan, M.B. Baker, L. Moroni, An efficient and easily adjustable heating stage for digital light processing set-ups, Addit. Manuf. 46 (2021), 102102, https://doi.org/10.1016/j.addma.2021.102102.
[37] Y. Zhang, Y. Li, V.K. Thakur, L. Wang, J. Gu, Z. Gao, B. Fan, Q. Wu, M.R. Kessler, Bio-based reactive diluents as sustainable replacements for styrene in MAESO resin, RSC Adv. 8 (2018) 13780–13788, https://doi.org/10.1039/c8ra00339d.
[38] Y. Yao, N. Sha, Z. Zhao, Highly concentrated hydroxyapatite suspension for DLP printing, IOP Conf. Ser. Mater. Sci. Eng. 678 (2019), 012016, https://doi.org/10.1088/1757-899X/678/1/012016.
[39] C. Hinczewski, S. Corbel, T. Chartier, Ceramic suspensions suitable for stereolithography, J. Eur. Ceram. Soc. 18 (1998) 583–590, https://doi.org/10.1016/s0955-2219(97)00186-6.
[40] L.E. Nielsen, R.F. Landel, Mechanical properties of polymers and composites, Marcel Dekker, Inc, New York, 1993.
[41] M. Kury, K. Ehrmann, G.A. Harak´aly, C. Gorsche, R. Liska, Low volatile monofunctional reactive diluents for radiation curable formulations, J. Polym. Sci. 59 (2021) 2154–2169, https://doi.org/10.1002/pol.20210171.
[42] T.J. Hammer, H.M.S. Mehr, C. Pugh, M.D. Soucek, Urethane methacrylate reactive diluents for UV-curable polyester powder coatings, J. Coat. Technol. Res. 18 (2021) 333–348, https://doi.org/10.1007/s11998-020-00391-8.
[43] Merck, Thermal Transitions of Homopolymers: Glass Transition & Melting Point, (2023). ⟨https://www.sigmaaldrich.com/IT/it/technical-documents/technical-article/materials-science-and-engineering/polymer-synthesis/thermal-transitions-of-homopolymers⟩ (accessed July 26, 2023).
[44] S. Cousinet, A. Ghadban, E. Fleury, F. Lortie, J.P. Pascault, D. Portinha, Toward replacement of styrene by bio-based methacrylates in unsaturated polyester resins, Eur. Polym. J. 67 (2015) 539–550, https://doi.org/10.1016/j.eurpolymj.2015.02.016.
[45] N. Roy, R. Sengupta, A.K. Bhowmick, Modifications of carbon for polymer composites and nanocomposites, Prog. Polym. Sci. 37 (2012) 781–819, https://doi.org/10.1016/j.progpolymsci.2012.02.002.
[46] A. Ferrreira, J.G. Rocha, A. Anso´n-Casaos, M.T. Martínez, F. Vaz, S. Lanceros-Mendez, Electromechanical performance of poly(vinylidene fluoride)/carbon nanotube composites for strain sensor applications, Sens. Actuators, A Phys. 178 (2012) 10–16, https://doi.org/10.1016/j.sna.2012.01.041.
[47] A. Ortega, B. Park, N.S. Kim, Printability and electrical conductivity of UV curable MWCNT ink, J. Electron. Mater. 44 (2015) 778–783, https://doi.org/10.1007/s11664-014-3468-8.
[48] E.E. Uren˜a-Benavides, M.J. Kayatin, V.A. Davis, Dispersion and rheology of multiwalled carbon nanotubes in unsaturated polyester resin, Macromolecules 46 (2013) 1642–1650, https://doi.org/10.1021/ma3017844.
[49] V. Strongone, M. Bartoli, P. Jagdale, R. Arrigo, A. Tagliaferro, G. Malucelli, Preparation and characterization of UV-LED curable acrylic films containing biochar and/or multiwalled carbon nanotubes: effect of the filler loading on the rheological, thermal and optical properties, Polymers 12 (2020) 796, https://doi.org/10.3390/polym12040796.
[50] H. Lorenz, J. Fritzsche, A. Das, K.W. Sto¨ckelhuber, R. Jurk, G. Heinrich, M. Klüppel, Advanced elastomer nano-composites based on CNT-hybrid filler systems, Compos. Sci. Technol. 69 (2009) 2135–2143, https://doi.org/10.1016/j.compscitech.2009.05.014.
[51] P. Cardoso, J. Silva, D. Klosterman, J.A. Covas, F.W.J. van Hattum, R. Simoes, S. Lanceros-Mendez, The role of disorder on the AC and DC electrical conductivity of vapour grown carbon nanofibre/epoxy composites, Compos. Sci. Technol. 72 (2012) 243–247, https://doi.org/10.1016/j.compscitech.2011.11.008.
[52] G. Gonzalez, A. Chiappone, I. Roppolo, E. Fantino, V. Bertana, F. Perrucci, L. Scaltrito, F. Pirri, M. Sangermano, Development of 3D printable formulations containing CNT with enhanced electrical properties, Polym. (Guildf.) 109 (2017) 246–253, https://doi.org/10.1016/j.polymer.2016.12.051.
[53] Z. Spitalsky, D. Tasis, K. Papagelis, C. Galiotis, Carbon nanotube-polymer composites: chemistry, processing, mechanical and electrical properties, Prog. Polym. Sci. 35 (2010) 357–401, https://doi.org/10.1016/j.progpolymsci.2009.09.003.
[54] M. Sangermano, E. Borella, A. Priola, M. Messori, R. Taurino, P. Po¨tschke, Use of single-walled carbon nanotubes as reinforcing fillers in UV-curable epoxy systems, Macromol. Mater. Eng. 293 (2008) 708–713, https://doi.org/10.1002/mame.200800126.
[55] Y.L. Huang, C.C.M. Ma, S.M. Yuen, C.Y. Chuang, H.C. Kuan, C.L. Chiang, S.Y. Wu, Effect of maleic anhydride modified MWCNTs on the morphology and dynamic mechanical properties of its PMMA composites, Mater. Chem. Phys. 129 (2011) 1214–1220, https://doi.org/10.1016/j.matchemphys.2011.06.020.
[56] P. Costa, S. Gonçalves, H. Mora, S.A.C. Carabineiro, J.C. Viana, S. Lanceros-Mendez, Highly sensitive piezoresistive graphene-based stretchable composites for sensing applications, ACS Appl. Mater. Interfaces 11 (2019) 46286–46295, https://doi.org/10.1021/acsami.9b19294.
[57] S.N. Tripathi, S. Singh, R.S. Malik, V. Choudhary, Effect of multiwalled carbon nanotubes on the properties of poly(methyl methacrylate) in PMMA/CNT nanocomposites, Macromol. Symp. 341 (2014) 75–89, https://doi.org/10.1002/masy.201400012.
[58] A. Chiappone, A. Pedico, S. Porcu, C.F. Pirri, A. Lamberti, I. Roppolo, Photocurable 3D-printable systems with controlled porosity towards CO_2 air filtering applications, Polym. (Basel) 14 (2022) 5265, https://doi.org/10.3390/polym14235265.
[59] N. Zohdi, R.C. Yang, Material anisotropy in additively manufactured polymers and polymer composites: a review, Polymers 13 (2021) 3368, https://doi.org/10.3390/polym13193368.
[60] R. Paz, R. Moriche, M. Monzo´n, J. García, Influence of manufacturing parameters and post processing on the electrical conductivity of extrusion-based 3D printed nanocomposite parts, Polymers 12 (2020) 733, https://doi.org/10.3390/POLYM12040733.
[61] K. Dembek, B. Podsiadły, M. Słoma, Influence of process parameters on the resistivity of 3D printed electrically conductive structures, Micromachines 13 (2022) 1203, https://doi.org/10.3390/mi13081203.
[62] J. Galos, Y. Hu, A.R. Ravindran, R.B. Ladani, A.P. Mouritz, Electrical properties of 3D printed continuous carbon fibre composites made using the FDM process, Compos. Part A Appl. Sci. Manuf. 151 (2021), 106661, https://doi.org/10.1016/j.compositesa.2021.106661.